energies

MDPI

Article

Operation Control and Performance Analysis of an Ocean Thermal Energy Conversion System Based on the Organic Rankine Cycle

Xiaowei Yang [1,2], Yanjun Liu [1,2,*], Yun Chen [1,2] and Li Zhang [3]

[1] Institute of Marine Science and Technology, Shandong University, Qingdao 266237, China; 201611637@mail.sdu.edu.cn (X.Y.); chenyuneast@mail.sdu.edu.cn (Y.C.)
[2] Key Laboratory of High Efficiency and Clean Mechanical Manufacture, Ministry of Education, School of Mechanical Engineering, Shandong University, Jinan 250061, China
[3] Southern Marine Science and Engineering Guangdong Laboratory (Zhanjiang), Zhanjiang 524000, China; zhangl@zjblab.com
* Correspondence: lyj111yjslw@163.com; Tel.: +86-133-2513-6508

Abstract: The development and utilization of marine renewable energy is an important measure for achieving energy conservation, emissions reduction and carbon neutrality. Ocean thermal energy is the most stable energy among all the types of marine renewable energy. This paper built a simulation model of an ocean thermal energy conversion system based on actual device specifications by Aspen and MATLAB and put forward a corresponding control strategy. The opening control signal of the control valve at the turbine inlet was the condenser inlet pressure in this paper, and the frequency control of the working fluid pump depended on the evaporating pressure and flow rate of the working fluid. This paper analyzed the key operating parameter changes of the system under different working conditions. According to the analysis results, the turbogenerator in this system was able to generate 50 kW power for about 8 months per year. The highest net output power of the Organic Rankine Cycle was 47.3 kW; the highest cycle thermal efficiency was 3.2%.

Keywords: ocean thermal energy; organic Rankine cycle; MATLAB; Aspen Plus

Citation: Yang, X.; Liu, Y.; Chen, Y.; Zhang, L. Operation Control and Performance Analysis of an Ocean Thermal Energy Conversion System Based on the Organic Rankine Cycle. *Energies* **2022**, *15*, 3971. https://doi.org/10.3390/en15113971

Academic Editors: Tzu-Chen Hung, Yong-Qiang Feng, Huan Xi and Pavel A. Strizhak

Received: 11 April 2022
Accepted: 18 May 2022
Published: 27 May 2022

1. Introduction

Energy conservation and emissions reduction are important measures for alleviating the energy and environmental crisis. Marine renewable energy is a clean form of energy with zero emissions. In practical applications, marine renewable energy power stations can provide reliable power for remote islands and deep-sea farming bases. A 5 MW power station can meet the electricity demands of a small, developing island state [1]. Due to the small temperature differences (only 0.4 °C [2]) in the surface seawater between day and night, ocean thermal energy is the most stable of all the types of marine renewable energy. In addition to power generation, ocean thermoelectric power stations can also be used for freshwater preparation, deep sea aquaculture and the refrigeration and extraction of deep-sea minerals, etc. [1]. Therefore, ocean thermal energy is considered to be an energy source with development potential.

So far, the research on ocean thermal energy conversion (OTEC) technology has mainly focused on different OTEC cycles [3,4], high-efficiency compact heat exchangers [5,6], turboexpanders [7,8], working fluids [9], economic analyses [10,11] and off-design performance research [12].

In terms of the different OTEC cycles, the thermal efficiency of the Guohai cycle is currently the highest, at about 5.1%, and the lowest is the Rankine cycle, at only 3.1% [13]. Other cycles include the Karina cycle [14,15] and the Uehara cycle [16–18], whose efficiencies are between those of the Guohai cycle and the Rankine cycle. In addition, some

scholars [19–21] have used solar energy to increase the surface seawater temperature of OTEC power stations, thereby improving the circulation efficiency of the OTEC system. Some scholars [22,23] have also used geothermal energy as a high-temperature warm source (not surface seawater) and deep seawater to establish circulation systems. While improving the cycle efficiency, this power station can also obtain deep seawater.

Compared with all kinds of high-efficiency circulation systems, the Organic Rankine Cycle (ORC) is the only OTEC cycle that has been implemented in demonstration projects due to its simple structure and high reliability. In 1881, the French scientist Arsonval first proved the feasibility of ocean thermal energy conversion technology. His student Georges then built the first OTEC factory in 1930. In the application of OTEC technology, the technologies of the United States and Japan are relatively advanced. The first floating closed-power station was the mini-OTEC, established by the United States in Hawaii in 1979 [24]. This power station can generate 53 kW gross power and 18 kW net power. Japan built an ocean thermal power station with a gross power of 120 kW and a net power of 31.5 kW in Naura in 1982 [24].

In 2013, Japan built a 50 kW OTEC power station based on the ORC structure in Okinawa using R134a as a working fluid. The surface seawater temperature was 27 °C, and the deep seawater temperature was only 8.8 °C [25]. In 2014, the United States built a 100-kW demonstration power station in Hawaii and this power station was successfully connected to the grid in August 2015 [26]. In 2013, the French built an experimental prototype of an OTEC power station on Reunion Island. This prototype has entered the testing stage and can generate 15 kW equivalent power [27].

This paper built a simulation model based on actual device specifications by Aspen and MATLAB and simulated the operational performance of the equipment under the full conditions of ocean thermal energy. The target was to obtain the maximum output power of the turbine. This paper linked the control of the thermophysical parameters of the working fluid with the controllable parameters of the actual components (the frequency of pumping and the opening of the control valve).

2. Methods

2.1. Simulation Model

This paper established a 50-kW power generation system based on the Organic Rankine Cycle system. R134a was used as the circulating working fluid for this system.

Figure 1 is the flow chart of an ocean thermal energy conversion system based on the Organic Rankine Cycle. The four major components of the organic Rankine cycle are the evaporator, condenser, turbine and working fluid pump. The key characteristic parameters of the four main components are listed in Table 1. In addition, in engineering practice, pipes and pipe fittings are also an important component that cannot be ignored. Table 2 lists the key characteristic parameters of the pipe system.

The control valve in the turbine inlet was used to control the pressure at the condenser inlet; we called this the pressure control valve. The control valve in the evaporator inlet was used to control the liquid level height in the shell side of the flooded evaporator; we called this the liquid level control valve.

Figure 2 is the simulation model. The valve marked SHUTOFF in Figure 2 was a pneumatic butterfly valve used for quick shut-off for when the turbine required an emergency shutdown.

In order to improve the efficiency of the circulation system, the energy conversion efficiency of the turboexpander is often required to be relatively high. Centripetal turboexpanders are commonly used in ocean thermal energy conversion systems, and the isentropic efficiency can often reach about 85% or even higher [7]. We wrote the centripetal turbine function script in MATLAB and embedded it in Aspen Plus. The basic method was to use the User2 module to link the Excel template with Aspen Plus, and then, Excel could call the MATLAB program [28]. For the MATLAB program written for the centripetal turbine, we solved the mass conservation equations for the nozzle, impeller and diffuser

separately through the fsolve function of MATLAB. The corresponding equations are listed in Appendix A, which are cited from ref. [29]. In addition, the thermophysical parameters of working fluid were queried by calling NIST REFPROP in the MATLAB program [30].

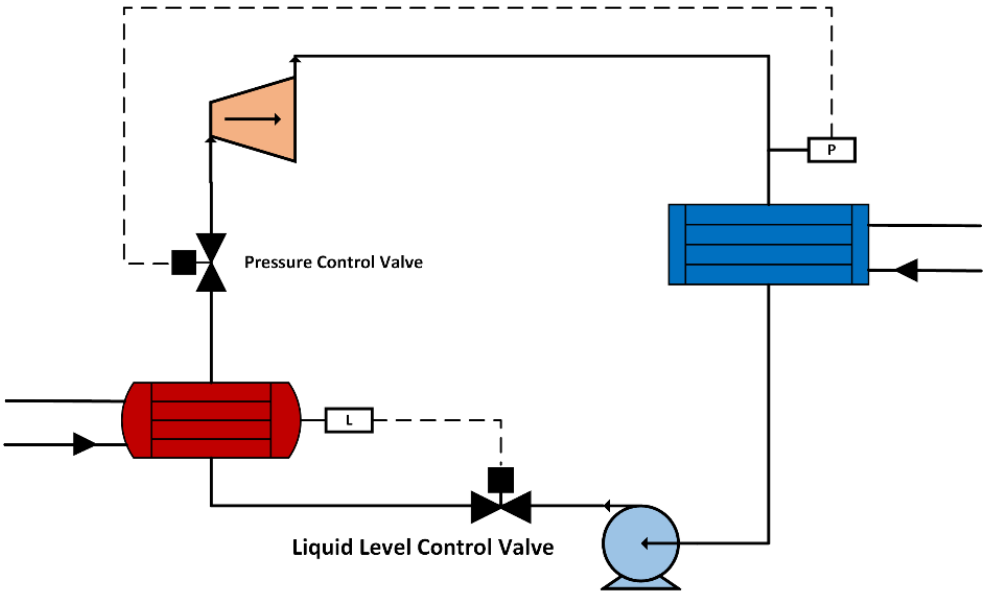

Figure 1. Flow chart of OTEC system based on ORC.

Table 1. The key characteristic parameters of the OTEC system.

Component	Type	Parameter	Value
Evaporator	Flooded	Working fluid location Heat exchange area Tube Type Tube Material	Shell side 301 m^2 Wieland 1575 fpm Al-Brass
Condenser	Shell and Tube	Working fluid location Heat exchange area Tube type Tube Material	Shell side 301 m^2 Wieland 1575 fpm Al-Brass
Pump	Canned Motor	Rated flow rate Rated head	24.2 m^3/h 31.8 m
Turbine	Centripetal	Rated speed Rated power	12,500 rpm 50 kW

Table 2. Detailed information for the pipe system.

Tube Location	Nominal Diameter	Pipe Rise	Pipe Length	Miscellaneous L/D
At turbine inlet	DN150	2 m	5.111 m	160
At condenser inlet	DN200	−0.564 m	6.075 m	140
At pump inlet	DN125	−1.9 m	2.47 m	95
At evaporator inlet	DN100	0	6.5 m	135

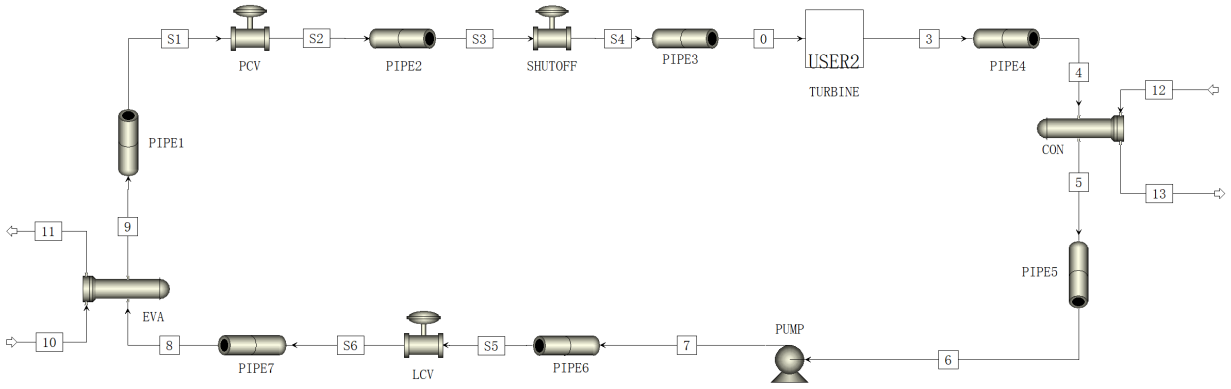

Figure 2. The Aspen Plus model. PCV: the pressure control valve; PIPE1~PIPE7: the pipe segment; SHUTOFF: the shut off valve; CON: the condenser; PUMP: the working fluid (R134a) pump; LCV: the control valve used for controlling liquid level in evaporator; EVA: the evaporator; 1~13 and S1~S6: the symbol mark of the inlet and outlet of each components.

2.2. Control Strategies and Components

Considering that the rectifier inverter system had overpower protection settings in the actual equipment, the maximum output power was limited to 50 kW in this study. When the system was able to generate 50 kW output power, under high surface seawater temperature conditions, control of the system required a constant power (50 kW) output from the turbogenerator. When the system was unable to generate 50 kW of power, under low surface seawater temperature conditions, control of the system required the maximum output power of the turbogenerator. The control strategy of the system consisted mainly of two aspects:

On the one hand, the opening control signal of the pressure control valve at the turbine inlet was the condenser inlet pressure in this paper. The reasons for this control strategy were as follows:

- There was no pipe fitting for adjustments in the pipe between the turbine outlet and the condenser inlet. The pipe structure and length were fixed. When the state parameters of the working fluid at one end of the pipeline and the flow parameters in the pipeline were determined, the state parameters of the working fluid at the other end are were determined. This is equivalent to indirectly controlling the turbine outlet pressure when the pressure control valve controls the condenser inlet pressure.
- The adjustment of the pressure control valve also affected the working fluid state parameters at the turbine inlet. This meant that the pressure control valve actively affected the state parameters of the three positions (turbine inlet and outlet and condenser inlet) at the same time.
- When the structure of a condenser was fixed, the heat exchange capacity of the condenser had an upper limit. If the condensing temperature was too low, meaning that the difference was small between the condensing temperature and the deep seawater temperature, the required deep seawater flow rate was too large when the heat exchange area was fixed. If the flow rate of the deep seawater was too large, the requirements for the deep seawater pump and deep seawater pipeline would be high, including structural size parameters, performance parameters and construction costs.

On the one hand, the frequency control of the working fluid pump is determined by the evaporating pressure and the flow rate of the working fluid. When the working fluid pump operates at a variable frequency, the ratio of the power consumption is equal to the cube of the ratio of the frequency. This method can also achieve the purpose of energy saving and improving the net output power.

For system control, the characteristics of the control valve and the variable frequency pump are particularly important. Figure 3 shows the characteristic curve of the ball valve and globe valve. Table 3 shows detailed information on the control valve.

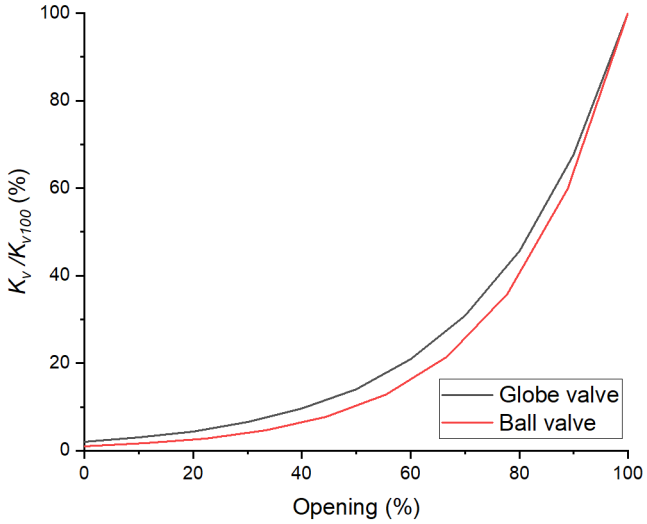

Figure 3. The control valve characteristic curve.

Table 3. Detailed information for the control valve.

Nominal Diameter	Type	K_{V100}	Installation Location
DN150	Ball	940	At the turbine inlet
DN80	Globe	100	At the evaporator inlet

K_V is the flow coefficient of the control valve, which is an index for measuring the flow capacity of the control valve. The K_{V100} is the rated K_V at a valve opening of 100%. A large flow coefficient value indicates that the flow capacity of the valve is large, and that the pressure loss of fluid flowing through the valve is small. The rated K_V is the flow coefficient at 100% opening of the control valve. The valve has different flow coefficients at different openings. The relationship between the flow coefficient and the opening is the valve characteristic curve that is obtained by the manufacturer's experimental test and provided to the user, as shown in Figure 3.

A ball valve was used as the pressure control valve in the turbine inlet here due to its higher-rated K_V. This high K_V value of the valve indicates a lower resistance.

The rated K_V of the butterfly valve was 1150. A globe valve was used as the liquid level control valve in the evaporator inlet. The liquid level control valve is used to control the liquid level height in a flooded evaporator. In this paper, the opening of the liquid level control valve was set to 80% in all working conditions. The liquid level control valve was only used for local fine-tuning of the evaporator liquid level when needed—for example, when the evaporating temperature and condensing temperature were artificially changed and the components' operating parameters changed drastically. When the ORC runs stably under a certain working condition, the opening of liquid level control valve is considered to remain unchanged.

Figure 4 shows the characteristic curves of the working fluid pump including the head, efficiency and net positive suction head required (NPSHr) characteristic curves. The characteristic curve of the pump was experimentally measured by the pump manufacturer Hermetic and provided to the user. The data that could be actually measured in the experiment included the power, volume flow rate, pressure of the working fluid at the inlet and outlet of the pump and the temperature of the working fluid. The density of working fluid was obtained by querying the thermophysical property database based on temperature and pressure. Then, according to the following formula, we were able to get the head and efficiency characteristic curve of the working fluid pump at different volume flow rates, as shown in Figure 4. According to the measured characteristic curve, we can know that head decreased with increases in volume flow rate, but the shaft power increased. Thus, there would be a peak in the efficiency calculated from the measured data.

In engineering, we determine the peak point of efficiency as the best operating conditions point and we preferably make the pump work in the high-efficiency zone of the pump's operation—that is, at more than 92% of its highest possible efficiency. When the volume flow rate reached 27 m^3/h, the pump efficiency reached its maximum value (59.76%). The volume flow rate range of the high-efficiency zone was 18.35–37.85 m^3/h and the mass flow rate was about 6.5–13.3 kg/s.

$$H = \frac{1000 * \Delta P}{\rho g} \tag{1}$$

$$N_{eff} = \frac{\rho g H Q}{3600 * 1000} = \frac{Q \Delta P}{3600} \tag{2}$$

$$\eta = \frac{N_{eff}}{N_{shaft}} = \frac{Q \Delta P}{3600 * N_{shaft}} \tag{3}$$

where, ΔP is the pressure difference, kPa; ρ is the density, kg/m^3; g = 9.8 m/s^2; Q is the volume flow rate, m^3/h; N_{eff} is the effective power, kW; N_{shaft} is the shaft power, kW; and NPSHr is an inherent characteristic of the pump, which represents the anti-cavitation performance of the pump. This means that the working fluid pump has good anti-cavitation impact performance when the value of NPSHr is small.

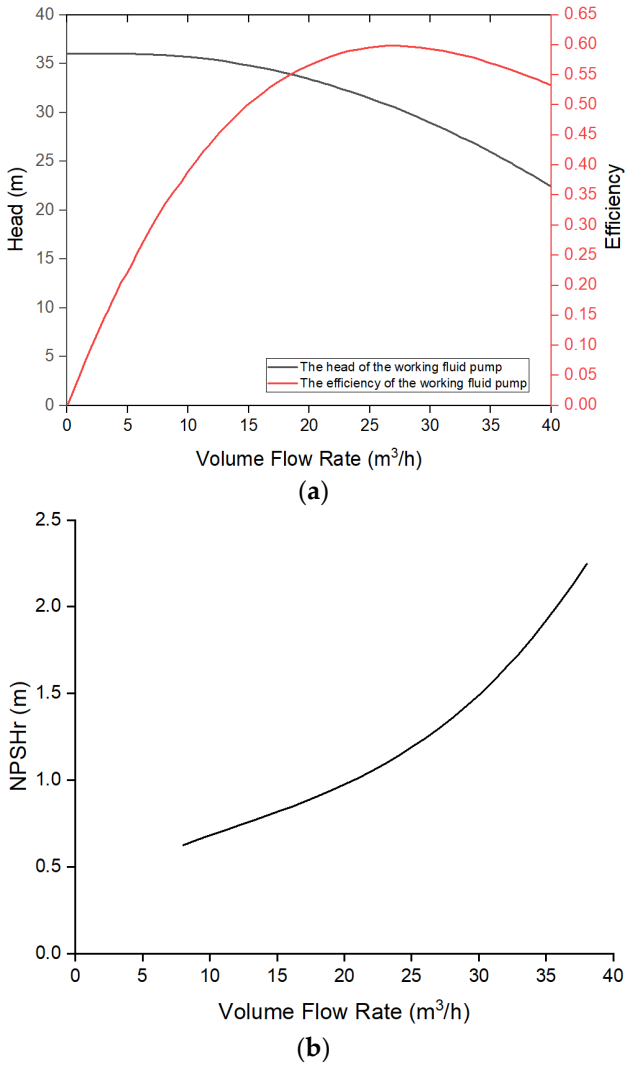

Figure 4. The characteristic curve of the working fluid pump. (**a**) Head and Efficiency vs. Volume Flow Rate. (**b**) NPSHr vs. Volume Flow Rate.

There is another parameter involved, the available net positive suction head (NPSHa), in the system analysis and calculations. The NPSHa is calculated from the liquid properties and the installation position of the working fluid pump compared to the condenser. In order to prevent the working fluid pump from being impacted by cavitation, it is necessary that NPSHa > NPSHr.

The value of the NPSHa can be increased by installing the pump below the condenser or increasing the subcooling degree of the working fluid at the condenser outlet. However, this will increase the heat exchange area and the cost of condenser when increasing the subcooling degree at the condenser outlet. So, we installed the pump 1.9 m below the condenser to reduce the need for subcooling of the working fluid at the outlet of the condenser.

2.3. Simulation Condition Settings

This paper mainly assumed that the difference between the surface seawater temperature and the evaporating temperature was 4 °C, and that the difference between the deep seawater temperature and the condensing temperature was also 4 °C. When the surface seawater temperature was 25 °C, 26 °C, 27 °C, 28 °C, 29 °C and 30 °C, the evaporating temperature corresponded to 21 °C, 22 °C, 23 °C, 24 °C, 25 °C and 26 °C.

The saturation pressure at 8 °C of R134a was 387.61 kPa. The pressure loss on the shell side of condenser was about 3–5 kPa. Therefore, we set the condenser inlet pressure as 391 kPa in this paper by controlling the opening of the pressure control valve in the turbine inlet.

The evaporator used in this paper was a flooded evaporator and the working fluid was a saturated vapor phase at the evaporator outlet.

3. Results

Figure 5 shows the changes in the system output power and the mass flow rate of the working fluid with evaporating temperature. The turbine output power remained constant at 50 kW when the evaporating temperature was higher than 22.8 °C. The specific enthalpy difference of the working fluid increased as the evaporating temperature increased when the condensing temperature remained unchanged. The output power of the turbine is the product of specific enthalpy difference and mass flow rate of working fluid. So, the mass flow rate of working fluid decreased with increases in the evaporating temperature when the evaporating temperature was higher than 22.8 °C. When the evaporating temperature was lower than 22.8 °C, the turbine output power and working fluid flow rate decreased with decreases in the evaporating temperature. The specific enthalpy of the working fluid flowing from the evaporator outlet to the turbine inlet remained unchanged and the pressure decreased. The superheat degree of the working fluid increased as the pressure decreased. From Figure 6, we know that the opening of the control valve at the turbine inlet was relatively large when the evaporating temperature was lower than 22.7 °C, leading to the pressure drop from the evaporator outlet to the turbine inlet being relatively small. So, the superheat degree of the working fluid at the turbine inlet was relatively small. When the evaporating temperature was lower than 22.8 °C and the flow rate of the working fluid was higher than the value shown in Figure 5, the working fluid would liquefy in the turbine. This would cause the turbine to be damaged by a liquid hammer. In order to protect the turbine, we could only reduce the turbine output power and the flow rate of the working fluid when the evaporating temperature was lower than 22.8 °C. So, there was an inflection point in the working fluid flow rate at 22.8 °C.

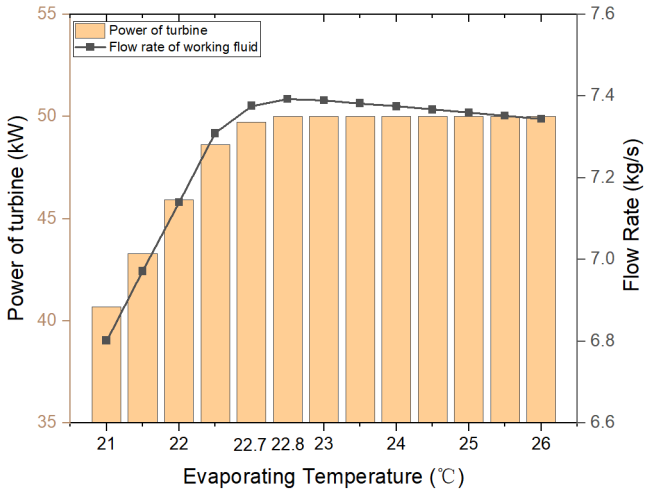

Figure 5. The output power and working fluid flow rate.

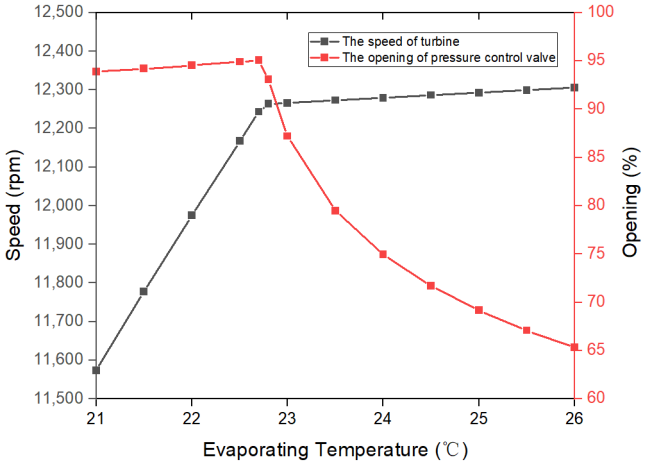

Figure 6. The speed of the turbine and the opening of the pressure control valve.

Figure 6 shows the changes in the turbine speed and the opening of the pressure control valve in the turbine inlet with the evaporating temperature. Combining Figures 5 and 6, we can see that when the evaporating temperature was higher than 22.8 °C, the flow rate of the working fluid changed little, and the opening of the pressure control valve in the turbine inlet changed greatly. This means that the stability of the turbine output power was mainly stabilized by the pressure control valve at the turbine inlet in this stage. When the evaporating temperature was lower than 22.8 °C, the output power of the turbine mainly depended on by the flow rate of the working fluid. Changes in the opening of the pressure control valve in the turbine inlet were relatively small.

In the ORC, the evaporating temperature and condensing temperature are artificially set parameters, and the working fluid flow rate is obtained according to the demands of turbine output power. The states of the working fluid are the saturated vapor state at the evaporator outlet and the saturated liquid state at the condenser outlet; that is, the pressure difference between the inlet and the outlet of the working fluid pump is known. At this time, the operating point of the working fluid pump and the frequency corresponding to this point can be determined based on the working fluid pump characteristic curve according to the flow rate and the pressure difference. Thus, the state parameters of the working fluid are known at each point of the entire ORC. That is, the heat duty that the working fluid needs to exchange with the seawater in heat exchanger is also known. The surface seawater and deep seawater flow rate are calculated by Aspen according to the energy balance.

From Figure 7, we can see that the temperature change of the surface seawater and deep seawater in the heat exchanger was basically stable under the various working conditions. When the evaporating temperature was higher than 22.8 °C, the heat duty increased slightly and the flow rate of the surface seawater decreased significantly. When the evaporating temperature was lower than 22.8 °C, the heat duty and flow rate of the surface seawater and deep seawater both increased with increases in the output power of the turbine.

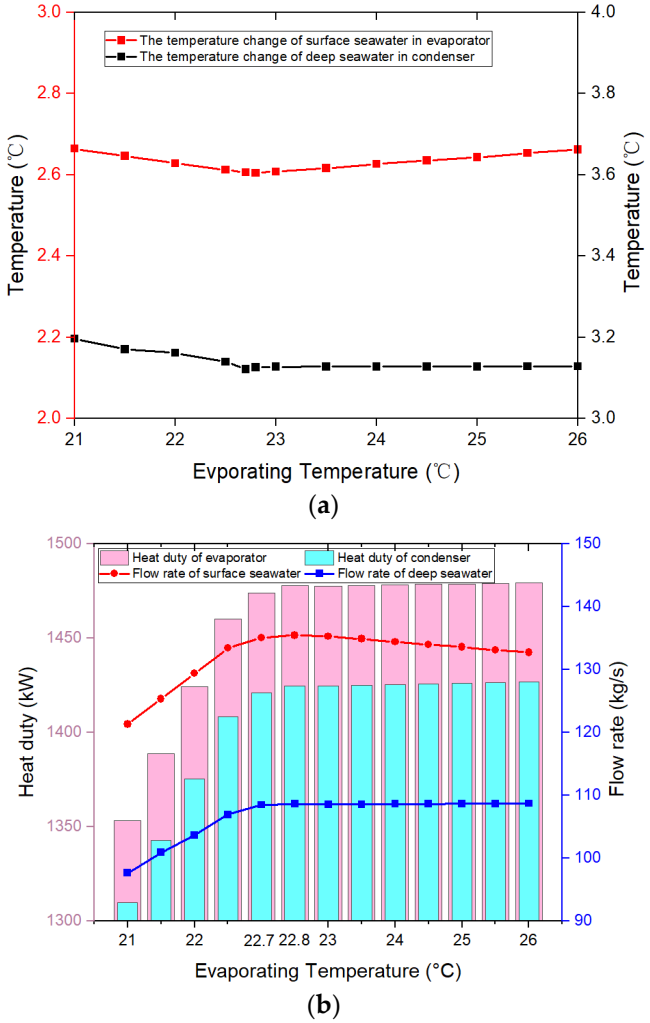

Figure 7. Analysis results for the surface seawater and deep seawater. (**a**) The temperature changes between the inlet and outlet of the evaporator/condenser for the surface seawater and deep seawater. (**b**) The heat duty of the evaporator/condenser and the flow rate of the surface/deep seawater.

In this study, the evaporating pressure was controlled by the variable frequency operation of the pump. At the same time, the frequency operation can also reduce the power consumption of the pump and improve the net output power of the system. Figure 8a shows the power consumption and operating frequency of the working fluid pump under various operating conditions. After simulation analysis, the pressure at the pump inlet was between 412.67 kPa and 412.98 kPa. The evaporating pressure increased as the evaporating temperature increased. Therefore, the pressure difference between the inlet and outlet of the working fluid pump also increased with increases in the evaporating temperature. The required head provided by the working fluid pump was increased. The head was proportional to the square of the frequency in the variable frequency operation of the pump. Therefore, the operating frequency of the working fluid pump also increased as the evaporating temperature increased. During variable frequency operation, the power of the

pump is proportional to the cube of the frequency. So, the power of pump also increased when the operating frequency increased. According to Figure 8b, the installation height of 1.9 m was enough to meet the requirement of NPSHa > NPSHr.

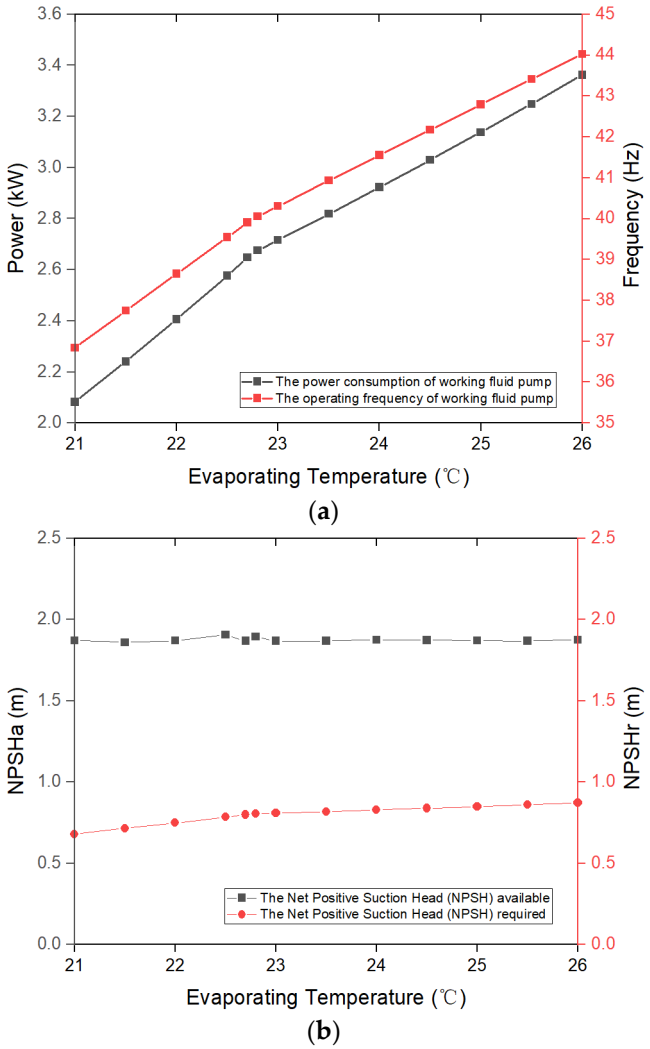

Figure 8. The results for the working fluid pump. (**a**) The power and operating frequency of the working fluid pump. (**b**) The NPSHa and NPSHr of the working fluid pump.

Figure 9 shows the output power and thermal efficiency of the circulation system under various working conditions. When the evaporating temperature was not lower than 22.8 °C, the turbine constantly output 50 kW of power. However, the power consumption of the working fluid pump continued to increase (in Figure 8) with increases in the evaporating temperature at this stage. Therefore, the net output power and thermal efficiency of the circulation system decreased with increases in the evaporating temperature at the 50 kW constant power output stage. According to the analysis results, the net output power and thermal efficiency of the circulation system both increased with increases in the evaporating temperature when the evaporating temperature was lower than 22.8 °C. The highest net output power was 47.3 kW and the highest cycle thermal efficiency was 3.2% when the evaporating temperature was 22.8 °C.

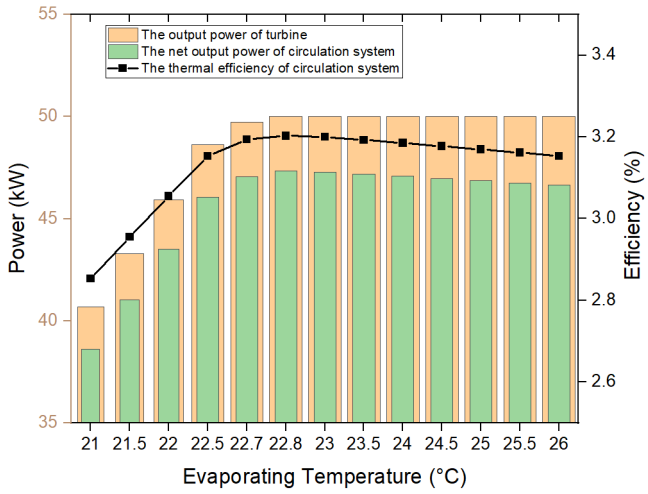

Figure 9. Thermal efficiency and output power of the circulation system.

Figure 10 shows the surface seawater temperature data in the South China Sea from 2012 to 2016 [31–35]. We can see that the OTEC system was able to generate 50 kW for about 8 months per year.

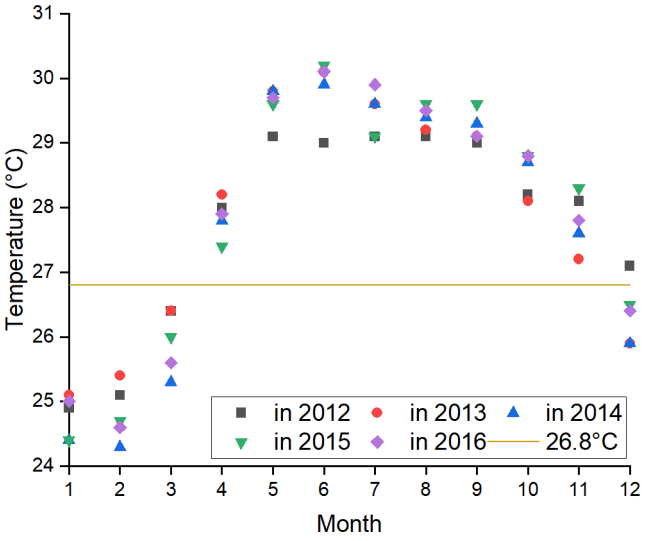

Figure 10. The monthly average surface seawater temperature in the South China Sea.

4. Conclusions

This paper built a simulation model of a 50 kW output power ocean thermal energy conversion system based on the Organic Rankine Cycle by Aspen Plus and MATLAB, and put forward a corresponding control strategy based on the limitations of the actual equipment, such as the overpower protection settings of the rectifier inverter system. After the simulation analysis, the following conclusions were obtained:

(1) When the evaporating temperature was not lower than 22.8 °C (the surface seawater temperature was not lower than 26.8 °C), the ORC system was able to output 50 kW of power stably. The maximum net power was 47.3 kW when the evaporating temperature was 22.8 °C; the maximum circulation thermal efficiency was 3.2% at this time. The OTEC system was able to generate 50 kW for about 8 months per year.

(2) The rated K_V value (K_{V100}) of the pressure control valve at the turbine inlet was 940 in this system. However, the maximum opening reached 95% when the evaporating temperature was 22.7 °C. The opening of the valve decreased with increases in the evaporating temperature when the evaporating temperature was above 22.8 °C, to ensure the

maximum constant output power of the turbine and the stability of the pressure at the turbine outlet.

(3) In regular design, the turbine inlet control valve is used to control the turbine speed. In actual operations, the valve meets the operational requirements when the turbine speed is stabilized in the range of 105% of the rated speed. Furthermore, if the turbine outlet pressure is too low, the temperature difference between the condensing temperature and the deep seawater temperature will be small, which results in the required condenser heat exchange area being larger than the actual area; this is not conducive to the safe and stable operation of the condenser. According to the analysis results, the control strategy of controlling the pressure in the condenser inlet had a great effect on stabilizing the rotational speed of the turbine in the constant power output stage. Therefore, we think that the pressure in the condenser inlet is more suitable as the control parameter of the control valve in the turbine inlet than turbine speed. This control method can not only stabilize the speed to a certain extent, but can also ensure the effective operation of the condenser.

Author Contributions: Conceptualization, methodology, software, validation, data curation and writing—original draft preparation, X.Y.; writing—review and editing, Y.L. and Y.C.; conceptualization, supervision and funding acquisition Y.L.; project administration, L.Z. All authors contributed to the design of the study. All authors have read and agreed to the published version of the manuscript.

Funding: This research was supported by the Fund of the Southern Marine Science and Engineering Guangdong Laboratory (Zhanjiang) Project (ZJW-2019-05).

Institutional Review Board Statement: Not applicable.

Informed Consent Statement: Not applicable.

Data Availability Statement: Not applicable.

Acknowledgments: Thanks to Yanjun Liu for his guidance and support.

Conflicts of Interest: The authors declare no conflict of interest.

Appendix A

The nozzle outlet is marked as point 1, the impeller outlet is marked as point 2, and the diffuser outlet is marked as point 3—which is the turbine outlet. Point 0 is the turbine inlet. The mathematical model was as follows:

The velocity and mass of working fluid at the nozzle outlet was:

$$c_1 = \sqrt{2\frac{k}{k-1}\frac{p_0}{\rho_0}\left[1-\left(\frac{p_1}{p_0}\right)^{\frac{n-1}{n}}\right]} = \sqrt{2h_1} \tag{A1}$$

$$n = \frac{k}{k-\varphi^2(k-1)} \tag{A2}$$

$$m_r = \rho_1 A_1 c_1 sin\alpha_1 \tag{A3}$$

where k is the adiabatic isentropic exponent, n is the adiabatic exponent, φ is the velocity coefficient in the nozzle, p is the pressure, A is the area, α_1 is the nozzle outlet angle, c is the absolute speed and h_1 is the specific enthalpy difference between the outlet and inlet of nozzle. Subscript 0 is the turbine inlet; 1 is the nozzle outlet.

The velocity and mass of the working fluid at the impeller outlet was:

$$u_1 = c_1 cos\alpha_1 \tag{A4}$$

$$u_2 = \mu u_1 \tag{A5}$$

$$w_1 = \sqrt{c_1^2 + u_1^2 - 2u_1 c_1 cos\alpha_1} \tag{A6}$$

$$q_B = \frac{4 * 0.1287 \rho_1 d_1^2 u_1^3}{m_r Re^{0.2}} \tag{A7}$$

$$c_2 = \sqrt{w_2^2 + u_2^2 - 2u_2 w_2 cos\beta_2} \tag{A8}$$

$$w_2 = \sqrt{\frac{2(1.0221 h_{2s} + 0.9779 q_B + 0.0221 h_1) + w_1^2 - u_1^2 + u_2^2}{\frac{1}{\psi^2} + 0.0221\left(\frac{1}{\psi^2} - 1\right)}} \tag{A9}$$

$$m_r = \rho_2 A_2 c_2 sin\alpha_2 \tag{A10}$$

where u is the circumferential speed of the impeller, μ is the ratio of the outlet and inlet diameter, w is the relative velocity, β_2 is the impeller outlet angle, h_{2s} is the isentropic enthalpy drop of the impeller outlet to the inlet, q_B is the impeller back friction loss, ψ is the velocity coefficient in the impeller, d is the diameter and Re is the Reynolds number. Subscript 2 is the impeller outlet.

The velocity and mass of working fluid at the diffuser outlet was:

$$c_3 = \sqrt{c_2^2 - 2\frac{k}{k-1}\frac{p_2}{\rho_2}\left[\left(\frac{p_3}{p_2}\right)^{\frac{k-1}{k\eta_K}} - 1\right]} \tag{A11}$$

$$m_r = \rho_3 A_3 c_3 sin\alpha_2 \tag{A12}$$

where η_K is the efficiency of the diffuser. Subscript 3 is the diffuser outlet.

An example of the program format for calling NIST REFPROP in MATLAB is as follows [30]:

$$i_{2s} = refpropm('H', 'P', p_2, 'S', s_1, 'R134a') \tag{A13}$$

which represents the isentropic specific enthalpy of the impeller outlet to the inlet. S and s are the specific entropy, H is the specific enthalpy and P is the pressure.

References

1. Magesh, R. OTEC technology—A world of clean energy and water. In Proceedings of the World Congress on Engineering, London, UK, 30 June–2 July 2010.
2. Chen, F. Research on Thermal Performance and Comprehensive Utilization of Ocean Thermoelectric Power Generation Device. Ph.D. Thesis, Harbin Engineering University, Harbin, China, 2016.
3. Semmari, H.; Stitou, D.; Mauran, S. A novel Carnot-based cycle for ocean thermal energy conversion. *Energy* **2012**, *43*, 361–375. [CrossRef]
4. Sun, F.; Zhou, W.; Nakagami, K. Energy-Economic Analysis and Configuration Design of the Kalina Solar-OTEC System. *Int. J. Comput. Electr. Eng.* **2013**, *5*, 187–191. [CrossRef]
5. Yasunaga, T.; Noguchi, T.; Morisaki, T. Basic heat exchanger performance evaluation method on OTEC. *J. Mar. Sci. Eng.* **2018**, *6*, 32. [CrossRef]
6. Fontaine, K.; Yasunaga, T.; Ikegami, Y. OTEC maximum net power output using Carnot cycle and application to simplify heat exchanger selection. *Entropy* **2019**, *21*, 1143. [CrossRef]
7. Chen, Y.; Liu, Y.; Zhang, L.; Yang, X. Three-Dimensional Performance Analysis of a Radial-Inflow Turbine for Ocean Thermal Energy Conversion System. *J. Mar. Sci. Eng.* **2021**, *9*, 287. [CrossRef]
8. Wu, Z.; Feng, H.; Chen, L. Optimal design of dual-pressure turbine in OTEC system based on constructal theory. *Energy Convers. Manag.* **2019**, *201*, 112179.1–112179.11. [CrossRef]
9. Yoon, J.I.; Son, C.H.; Baek, S.M. Efficiency comparison of subcritical OTEC power cycle using various working fluids. *Heat Mass Transf.* **2014**, *50*, 985–996. [CrossRef]
10. Seungtaek, L.; Hosaeng, L.; Junghyun, M. Simulation Data of Regional Economic Analysis of OTEC for Applicable Area. *Processes* **2020**, *8*, 1107. [CrossRef]
11. Bernardoni, C.; Binotti, M.; Giostri, A. Techno-economic analysis of closed OTEC cycles for power generation. *Renew. Energy* **2019**, *132*, 1018–1033. [CrossRef]
12. Giostri, A.; Romei, A.; Binotti, M. Off-design performance of closed OTEC cycles for power generation. *Renew. Energy* **2021**, *170*, 1353–1366. [CrossRef]
13. Liu, W.M.; Chen, F.Y.; Wang, Y.Q. Progress of Closed-Cycle OTEC and Study of a New Cycle of OTEC. *Adv. Mater. Res.* **2012**, *354–355*, 275–278. [CrossRef]
14. Kalina, A.I. Combined-Cycle System With Novel Bottoming Cycle. *ASME J. Eng. Turbines Power* **1984**, *106*, 737–742. [CrossRef]

15. Ren, H. Effect of Low Ammonia Mass Fraction of the Base Solution on Theoretical Cycle Efficiency of Kalina Cycle System (kcs-34). *J. Mech. Eng.* **2012**, *48*, 152. [CrossRef]
16. Ikegami, Y.; Yasunaga, T.; Harada, H. Performance Experiments on Ocean Thermal Energy Conversion System Using the Uehara Cycle. *Bull. Soc. Sea Water Sci. Jpn.* **2006**, *60*, 32–38.
17. Uehara, H.; Ikegami, Y.; Nishida, T. Performance Analysis of OTEC System Using a Cycle with Absorption and Extraction Processes. *Trans. Jpn. Soc. Mech. Eng.* **1998**, *64*, 2750–2755. [CrossRef]
18. Goto, S.; Motoshima, Y.; Sugi, T. Construction of simulation model for OTEC plant using Uehara cycle. *Electr. Eng. Jpn.* **2011**, *176*, 1–13. [CrossRef]
19. Aydin, H.; Lee, H.S.; Kim, H.J.; Shin, S.K.; Park, K. Off-design performance analysis of a closed-cycle ocean thermal energy conversion system with solar thermal preheating and superheating. *Renew. Energy* **2014**, *72*, 154–163. [CrossRef]
20. Park, S.; Chun, W.; Kim, N. Simulated production of electric power and desalination using Solar-OTEC hybrid system. *Int. J. Energy Res.* **2017**, *41*, 637–649. [CrossRef]
21. Cui, Q. Research on Solar-assisted Ocean Thermal Energy Conversion System. *IOP Conf. Ser. Earth Environ. Sci.* **2021**, *687*, 012137. [CrossRef]
22. Dugger, G.; Richards, D.; Paddison, F. Alternative ocean energy products and hybrid geothermal-OTEC/GEOTEC/plants. In Proceedings of the 2nd Terrestrial Energy Systems Conference, Colorado Springs, CO, USA, 1–3 December 1981; p. 2547.
23. Idrus, N.; Musa, M.N.; Yahya, W.J. Geo-Ocean Thermal Energy Conversion (GeOTEC) power cycle/plant. *Renew. Energy* **2017**, *111*, 372–380. [CrossRef]
24. Avery, W.H.; Wu, C. *Renewable Energy from the Ocean: A Guide to OTEC*; Oxford University Press: New York, NY, USA, 1994.
25. Yue, J.; Yu, T.; Li, D. The latest progress and development suggestions of ocean thermoelectric power generation technology at home and abroad. *J. Ocean. Technol.* **2017**, *36*, 6.
26. Makai Connects World's Largest Ocean Thermal Plant to U.S. Grid. August 2015 [EB/OL]. Available online: http://www.makai.com/makai-news/2015_08_29_makai_connects_otec/ (accessed on 11 April 2022).
27. Journoud, A.; Sinama, F.; Lucas, F. Experimental ocean thermal energy convemion (OTEC) project on the Reunion Island. In Proceedings of the 4th International Conference on Ocean Energy, Dublin, Ireland, 17–20 October 2012.
28. Fontalvo, J. Using user models in Matlab within the Aspen Plus interface with an Excel link. *Ing. Investig.* **2014**, *34*, 39–43. [CrossRef]
29. Ji, G. *Turboexpander*; Machinery Industry Press: Beijing, China, 1982.
30. Keith Wait. Linking REFPROP with Other Applications (Matlab Applications). Available online: https://trc.nist.gov/refprop/LINKING/Linking.htm#MatLabApplications (accessed on 11 April 2022).
31. Bulletin on the State of the Marine Environment in the South China Sea. 2012. Available online: http://scs.mnr.gov.cn/scsb/gbytj/201305/1f40063ea3404e9cbca7cd3d69e1b75e.shtml (accessed on 11 April 2022).
32. Bulletin on the State of the Marine Environment in the South China Sea. 2013. Available online: http://scs.mnr.gov.cn/scsb/gbytj/201408/635886a23e3d4a64b6d90b1ac1cc0e6b.shtml (accessed on 11 April 2022).
33. Bulletin on the State of the Marine Environment in the South China Sea. 2014. Available online: http://scs.mnr.gov.cn/scsb/gbytj/201505/381cf79ab8054fd6b4dcf67968b8202e.shtml (accessed on 11 April 2022).
34. Bulletin on the State of the Marine Environment in the South China Sea. 2015. Available online: http://scs.mnr.gov.cn/scsb/gbytj/201607/edc0f44a77e44eb1bd5893db10fa463e.shtml (accessed on 11 April 2022).
35. Bulletin on the State of the Marine Environment in the South China Sea. 2016. Available online: http://scs.mnr.gov.cn/scsb/gbytj/201706/e2cb33d595c74a22902c599c063d6b4c.shtml (accessed on 11 April 2022).